

## RESEARCH ARTICLE

# High-Order Algorithms for Compressible Reacting Flow with Complex Chemistry

M. Emmett<sup>a\*</sup>, W. Zhang<sup>a</sup>, and J. B. Bell<sup>a</sup>

<sup>a</sup>*Center for Computational Sciences and Engineering, Lawrence Berkeley National Laboratory, Berkeley, CA 94720.;*

*(Received 00 Month 200x; final version received 00 Month 200x)*

In this paper we describe a numerical algorithm for integrating the multicomponent, reacting, compressible Navier-Stokes equations, targeted for direct numerical simulation of combustion phenomena. The algorithm addresses two shortcomings of previous methods. First, it incorporates an eighth-order narrow stencil approximation of diffusive terms that reduces the communication compared to existing methods and removes the need to use a filtering algorithm to remove Nyquist frequency oscillations that are not damped with traditional approaches. The methodology also incorporates a multirate temporal integration strategy that provides an efficient mechanism for treating chemical mechanisms that are stiff relative to fluid dynamical time scales. The overall methodology is eighth order in space with option for fourth order to eighth order in time. The implementation uses a hybrid programming model designed for effective utilization of many-core architectures. We present numerical results demonstrating the convergence properties of the algorithm with realistic chemical kinetics and illustrating its performance characteristics. We also present a validation example showing that the algorithm matches detailed results obtained with an established low Mach number solver.

**Keywords:** DNS; spectral deferred corrections; finite difference; high-order methods; flame simulations

## 1. Introduction

The simulation of a turbulent reacting flow without the use of either turbulence models or closure models for turbulence chemistry interaction is referred to as a direct numerical simulation, or DNS. One of the standard computational tools used in DNS studies of combustion is the numerical integration of the multicomponent, reacting compressible Navier-Stokes equations. DNS approaches have been in active use in the combustion community for more than twenty-five years; a comprehensive review of the literature is outside the scope of this article. Examples of early work in the field can be found in [3, 8, 14, 16, 27, 37]. With the advent of massively parallel, high performance computer architectures, it is now feasible to perform fully compressible DNS simulations for turbulent flows with detailed kinetics. See, for example, [20, 30, 34, 39].

Compressible DNS approaches place a premium on high orders of accuracy. Spatial discretizations are typically based on defining high-order spatial derivative operators,  $D_x$ ,  $D_y$  and  $D_z$ . Common choices are central difference approximations [18] or compact differences based on Pade approximations [22]. Two codes that have seen significant application in combustion, SENGAL [7, 16] and S3D [20, 31, 39],

---

\*Corresponding author. Email: MWE Emmett@lbl.gov

use tenth and eighth order central differences, respectively. Second-order derivative terms are approximated using repeated application of the first-order derivative operators, namely

$$(a(x)U_x)_x \approx D_x(aD_xU)$$

This treatment of second-order derivatives does not provide adequate damping for Nyquist-frequency oscillations. Consequently some type of higher-order filter is employed periodically to damp high-frequency components of the system. Alternatively, the chain rule can be applied to second-order derivative terms. However, the chain rule approach is known to have stability issues (see e.g., [17]). Discretization of the spatial operators results in a system of ordinary differential equations (ODEs), which are typically integrated using high-order explicit Runge Kutta schemes such as those discussed by Kennedy *et al.* [19].

Although these types of compressible DNS codes have been highly successful, they suffer from two basic weaknesses. First, the use of explicit integration techniques limits the time step to the minimum of acoustic and chemical time scales. (Diffusive time scales are typically less restrictive than acoustic time scales for DNS.) This can be particularly restrictive for detailed chemical kinetics that can be stiff on acoustic time scales. The time step restriction can be relaxed by using an implicit / explicit temporal integration scheme such as IMEX but at the expense of solving linear systems to implicitly advance the kinetics at acoustic time scales.

The other issue with traditional compressible DNS methodology is the evaluation of second-order derivative terms by repeated application of the high-order first derivative operators. This approach is efficient in terms of floating point work but requires multiple communication steps for each evaluation of the spatial operators. Although this type of design has been effective, as we move toward new many-core architectures that place a premium on reduced communication, the algorithm becomes communication bound and computational efficiency is reduced.

In this paper, we introduce two new algorithm features that address the weaknesses discussed above. For the spatial discretization, we introduce an extension of the sixth-order narrow stencil finite difference algorithm of Kamakoti and Pantano [17] that provides a single discretization of  $(a(x)U_x)_x$  to eighth-order accuracy. This approach requires significantly more floating point work than the standard approach but allows the spatial discretization to be computed with a single communication step. Furthermore, it eliminates the need for a filter to damp Nyquist-frequency oscillations. We also introduce a multirate time stepping strategy based on spectral deferred corrections (SDC) that enables the chemistry to be advanced on a different time scale than the fluid dynamics. This allows the fluid dynamics to be evaluated less frequently than in a fully coupled code resulting in shorter run times. These algorithms are implemented in a hybrid OpenMP/MPI parallel code named **SMC**.

In §2 we introduce the spatial discretization used by **SMC** and the eighth-order narrow stencil discretization operators. In §3 we discuss the temporal discretization used by **SMC** and the multirate spectral deferred correction algorithm. In §4 we discuss some of the issues associated with a hybrid parallel implementation of **SMC**. In particular, we discuss a spatial blocking strategy that provides effective use of OpenMP threads. In §5 we present numerical results illustrating the convergence properties and parallel performance of **SMC**, and show its application to dimethyl ether-air combustion. Finally, the main results of the paper are summarized in §6.

## 2. Spatial Discretization

### 2.1 Navier-Stokes Equations

The reacting compressible Navier-Stokes equations are given by

$$\frac{\partial \rho}{\partial t} + \nabla \cdot (\rho \mathbf{u}) = 0, \quad (1a)$$

$$\frac{\partial \rho \mathbf{u}}{\partial t} + \nabla \cdot (\rho \mathbf{u} \mathbf{u}) + \nabla p = \nabla \cdot \boldsymbol{\tau}, \quad (1b)$$

$$\frac{\partial \rho Y_k}{\partial t} + \nabla \cdot (\rho Y_k \mathbf{u}) = \rho \dot{\omega}_k - \nabla \cdot \mathcal{F}_k, \quad (1c)$$

$$\frac{\partial \rho E}{\partial t} + \nabla \cdot [(\rho E + p) \mathbf{u}] = \nabla \cdot (\lambda \nabla T) + \nabla \cdot (\boldsymbol{\tau} \cdot \mathbf{u}) - \nabla \cdot \sum_k \mathcal{F}_k h_k, \quad (1d)$$

where  $\rho$  is the density,  $\mathbf{u}$  is the velocity,  $p$  is the pressure,  $E$  is the specific energy density (kinetic energy plus internal energy),  $T$  is the temperature,  $\boldsymbol{\tau}$  is the viscous stress tensor,  $\lambda$  is the thermal conductivity. For each of the chemical species  $k$ ,  $Y_k$  is the mass fraction,  $\mathcal{F}_k$  is the diffusive flux,  $h_k$  is the specific enthalpy, and  $\dot{\omega}_k$  is the production rate. The system is closed by an equation of state that specifies  $p$  as a function of  $\rho$ ,  $T$  and  $Y_k$ . For the examples presented here, we assume an ideal gas mixture.

The viscous stress tensor is given by

$$\tau_{ij} = \eta \left( \frac{\partial u_i}{\partial x_j} + \frac{\partial u_j}{\partial x_i} - \frac{2}{3} \delta_{ij} \nabla \cdot \mathbf{u} \right) + \xi \delta_{ij} \nabla \cdot \mathbf{u}, \quad (2)$$

where  $\eta$  is the shear viscosity and  $\xi$  is the bulk viscosity.

A mixture model for species diffusion is employed in SMC. We define an initial approximation  $\bar{\mathcal{F}}_k$  to the species diffusion flux given by

$$\bar{\mathcal{F}}_k = -\rho D_k \left( \nabla X_k + (X_k - Y_k) \frac{\nabla p}{p} \right) \quad (3)$$

where  $X_k$  is the mole fraction, and  $D_k$  is the diffusion coefficient of species  $k$ . For species transport to be consistent with the principle of conservation of mass we require

$$\sum_k \mathcal{F}_k = 0. \quad (4)$$

In general, the fluxes defined by (3) do not satisfy this requirement and some type of correction is required. When there is a good choice for a reference species that has a high molar concentration throughout the entire domain, one can use (3) to define the species diffusion flux (i.e.,  $\mathcal{F}_k \equiv \bar{\mathcal{F}}_k$ ) for all species except the reference, and then use (4) to define the flux of the reference species. This strategy is often used in combustion using  $\text{N}_2$  as the reference species. An alternative approach [29] is to define a correction velocity  $\mathbf{V}_c$  given by

$$\mathbf{V}_c = \sum_{\ell} \bar{\mathcal{F}}_{\ell} \quad (5)$$

and then to set

$$\mathcal{F}_k = \bar{\mathcal{F}}_k - Y_k \mathbf{V}_c. \quad (6)$$

The SMC code supports both of these operating modes. We will discuss these approaches further in §2.3.

## 2.2 Eighth-Order and Sixth-Order Discretization

The SMC code discretizes the governing Navier-Stokes equations (1) in space using high-order centered finite-difference methods. For first order derivatives a standard 8<sup>th</sup> order stencil is employed. For second order derivatives with variable coefficients of the form

$$\frac{\partial}{\partial x} \left( a(x) \frac{\partial u}{\partial x} \right), \quad (7)$$

a novel 8<sup>th</sup> order narrow stencil is employed. This stencil is an extension of those developed by Kamakoti and Pantano [17]. The derivatives in (7) on a uniform grid are approximated by

$$\frac{\partial}{\partial x} \left( a \frac{\partial u}{\partial x} \right) \Big|_i \approx \frac{H_{i+1/2} - H_{i-1/2}}{\Delta x^2}, \quad (8)$$

where

$$H_{i+1/2} = \sum_{m=-s+1}^s \sum_{n=-s+1}^s a_{i+m} M_{mn} u_{i+n}, \quad (9)$$

$s = 4$ , and  $M$  is an  $8 \times 8$  matrix (in general, for a discretization of order  $2s$ ,  $M$  is a  $2s \times 2s$  matrix). This discretization is conservative because (8) is in flux form. Note, however, that  $H_{i+1/2}$  is not a high-order approximation of the flux at  $x_{i+1/2}$  even though the flux difference (8) approximates the derivative of the flux to order  $2s$ . This type of stencil is *narrow* because the width of the stencil is only  $2s + 1$  for both  $u$  and  $a$ . In contrast, the width of a wide stencil in which the first-order derivative operator is applied twice is  $4s + 1$  for  $u$  and  $2s + 1$  for  $a$ .

Following the strategy in [17], a family of 8<sup>th</sup> order narrow stencils for the second order derivative in (7) has been derived. The resulting 8<sup>th</sup> order stencil matrix is given by

$$M = \begin{bmatrix} m_{11} & m_{12} & m_{13} & m_{14} & m_{15} & 0 & 0 & 0 \\ m_{21} & m_{22} & m_{23} & m_{24} & m_{25} & m_{26} & 0 & 0 \\ m_{31} & m_{32} & m_{33} & m_{34} & m_{35} & m_{36} & m_{37} & 0 \\ m_{41} & m_{42} & m_{43} & m_{44} & m_{45} & m_{46} & m_{47} & m_{48} \\ -m_{48} & -m_{47} & -m_{46} & -m_{45} & -m_{44} & -m_{43} & -m_{42} & -m_{41} \\ 0 & -m_{37} & -m_{36} & -m_{35} & -m_{34} & -m_{33} & -m_{32} & -m_{31} \\ 0 & 0 & -m_{26} & -m_{25} & -m_{24} & -m_{23} & -m_{22} & -m_{21} \\ 0 & 0 & 0 & -m_{15} & -m_{14} & -m_{13} & -m_{12} & -m_{11} \end{bmatrix}, \quad (10)$$

where

$$\begin{aligned}
m_{11} &= \frac{5}{336} + m_{48}, & m_{12} &= -\frac{83}{3600} - \frac{1}{5}m_{47} - \frac{14}{5}m_{48}, \\
m_{13} &= \frac{299}{50400} + \frac{2}{5}m_{47} + \frac{13}{5}m_{48}, & m_{14} &= \frac{17}{12600} - \frac{1}{5}m_{47} - \frac{4}{5}m_{48}, \\
m_{15} &= \frac{1}{1120}, & m_{21} &= -\frac{11}{560} - 2m_{48}, \\
m_{22} &= -\frac{31}{360} + m_{47} + 3m_{48}, & m_{23} &= \frac{41}{200} - \frac{9}{5}m_{47} + \frac{4}{5}m_{48}, \\
m_{24} &= -\frac{5927}{50400} + \frac{4}{5}m_{47} - \frac{9}{5}m_{48}, & m_{25} &= \frac{17}{600} - \frac{1}{5}m_{47} - \frac{4}{5}m_{48}, \\
m_{26} &= -\frac{503}{50400} + \frac{1}{5}m_{47} + \frac{4}{5}m_{48}, & m_{31} &= -\frac{1}{280}, \\
m_{32} &= \frac{1097}{5040} - 2m_{47} + 6m_{48}, & m_{33} &= -\frac{1349}{10080} + 3m_{47} - 12m_{48}, \\
m_{34} &= -\frac{887}{5040} - m_{47} + 6m_{48}, & m_{35} &= \frac{3613}{50400} + \frac{4}{5}m_{47} - \frac{9}{5}m_{48}, \\
m_{36} &= \frac{467}{25200} - \frac{3}{5}m_{47} + \frac{18}{5}m_{48}, & m_{37} &= \frac{139}{25200} - \frac{1}{5}m_{47} - \frac{9}{5}m_{48}, \\
m_{41} &= \frac{17}{1680} + 2m_{48}, & m_{42} &= -\frac{319}{2520} + 2m_{47} - 8m_{48}, \\
m_{43} &= -\frac{919}{5040} - 2m_{47} + 6m_{48}, & m_{44} &= -\frac{445}{2016}, \\
m_{45} &= \frac{583}{720} - m_{47} + 6m_{48}, & m_{46} &= -\frac{65}{224} - 7m_{48},
\end{aligned}$$

and  $m_{47}$  and  $m_{48}$  are two free parameters. Note that the well-posedness requirement established in [17] is satisfied by the stencil matrix above independent of the two free parameters. Furthermore, the leading order term of the truncation error contains an additive term that is independent of the free parameters, and hence the accuracy of the stencil is not sensitive to the choice of the two free parameters. As such, in SMC the free parameters were set to  $m_{47} = 3557/44100$  and  $m_{48} = -2083/117600$  to minimize the truncation error when the high-frequency modes of  $u$  and  $a$  are of similar magnitude.

The SMC code uses a 6<sup>th</sup> order stencil near physical boundaries where the conditions outside the domain are not well specified (see §2.4). The general 6<sup>th</sup> order stencil matrix is given by

$$M = \begin{bmatrix} m_{11} & m_{12} & m_{13} & m_{14} & 0 & 0 \\ m_{21} & m_{22} & m_{23} & m_{24} & m_{25} & 0 \\ m_{31} & m_{32} & m_{33} & m_{34} & m_{35} & m_{36} \\ -m_{36} & -m_{35} & -m_{34} & -m_{33} & -m_{32} & -m_{31} \\ 0 & -m_{25} & -m_{24} & -m_{23} & -m_{22} & -m_{21} \\ 0 & 0 & -m_{14} & -m_{13} & -m_{12} & -m_{11} \end{bmatrix}, \quad (11)$$

where

$$m_{11} = -\frac{11}{180} + m_{36}, \quad m_{12} = \frac{1}{9} - 2m_{36},$$

$$\begin{aligned}
m_{13} &= -\frac{1}{18} + m_{36}, & m_{14} &= \frac{1}{180}, \\
m_{21} &= \frac{7}{60} - 3m_{36}, & m_{22} &= -\frac{1}{120} + 5m_{36}, \\
m_{23} &= -\frac{17}{90} - 2m_{36}, & m_{24} &= \frac{5}{72} + m_{36}, \\
m_{25} &= \frac{1}{90} - m_{36}, & m_{31} &= -\frac{1}{15} + 3m_{36}, \\
m_{32} &= -\frac{11}{60} - 3m_{36}, & m_{33} &= -\frac{101}{360}, \\
m_{34} &= \frac{137}{180} - 2m_{36}, & m_{35} &= -\frac{83}{360} + m_{36},
\end{aligned}$$

and  $m_{36}$  is a free parameter. The 6<sup>th</sup> order narrow stencil developed in [17] is a special case of the general 6<sup>th</sup> order stencil when  $m_{36} = 0.220063$ . Like the 8<sup>th</sup> order stencil, the well-posedness and the order of accuracy for the 6<sup>th</sup> order stencil is independent of the free parameter. In SMC, the free parameter is set to  $281/3600$  to minimize the truncation error when the high-frequency modes of  $u$  and  $a$  are of similar magnitude.

### 2.3 Correction for Species Diffusion

In §2.1, we introduced the two approaches employed in SMC to enforce the consistency of the mixture model of species diffusion with respect to mass conservation. The first approach uses a reference species and is straightforward to implement. We note that the last term in (1d) can be treated as  $-\nabla \cdot \sum_k \mathcal{F}_k (h_k - h_{\text{ref}})$ , where  $h_{\text{ref}}$  is the species enthalpy for the reference species, because of (4). The second approach uses a correction velocity (5) and involves the computation of  $\nabla \cdot (Y_k \mathbf{V}_c)$  and  $\nabla \cdot (h_k Y_k \mathbf{V}_c)$ . Although one might attempt to compute the correction velocity according to  $V_{c,i+1/2} = \sum_\ell H_{\ell,i+1/2}$ , where  $H_{\ell,i+1/2}$  for species  $\ell$  is computed using (9), this would reduce the accuracy for correction velocity to second-order since  $H_{i+1/2}$  is only a second-order approximation to the flux at  $i+1/2$ . To maintain 8<sup>th</sup> order accuracy without incurring extra communication and too much extra computation, we employ the chain rule for the correction terms. For example, we compute  $\nabla \cdot (h_k Y_k \mathbf{V}_c)$  as  $h_k Y_k \nabla \cdot \mathbf{V}_c + \nabla (h_k Y_k) \cdot \mathbf{V}_c$ , and use  $\nabla \cdot \mathbf{V}_c = \sum_\ell \nabla \cdot \bar{\mathcal{F}}_\ell$ , where  $\nabla \cdot \bar{\mathcal{F}}_\ell$  is computed using the 8<sup>th</sup> order narrow stencil for second order derivatives. By default, we use the second approach because the first approach may result in unphysical diffusion in the reference species that absorbs all the errors in species diffusion fluxes.

### 2.4 Physical Boundaries

The SMC code uses characteristic boundary conditions to treat physical boundaries. Previous studies in the literature have shown that characteristic boundary conditions can successfully lower acoustic reflections at open boundaries without suffering from numerical instabilities. Thompson [35, 36] applied the one-dimensional approximation of the characteristic boundary conditions to the hyperbolic Euler equations, and the one-dimensional formulation was extended by Poinot and Lele [28] to the viscous Navier-Stokes equations. For multicomponent reacting flows, Sutherland and Kennedy [33] further improved the treatment of boundary conditions by the inclusion of reactive source terms in the formulation. In SMC, we have

adopted the formulation of characteristic boundary conditions proposed in [38, 40], in which multi-dimensional effects are also included.

The 8<sup>th</sup> order stencils used in **SMC** require four cells on each side of the point where the derivative is being calculated. Near the physical boundaries where the conditions outside the domain are unknown, lower order stencils are used for derivatives with respect to the normal direction. At the fourth and third cells from the boundary we use 6<sup>th</sup> and 4<sup>th</sup> order centered stencils respectively, for both advection and diffusion. At cells next to the boundary we reduce to centered second-order for diffusion and a biased third-order discretization for advection. Finally, for the boundary cells, a completely biased second-order stencil is used for diffusion and a completely biased third-order stencil is used for advection.

### 3. Temporal Discretization

#### 3.1 Spectral Deferred Corrections

SDC methods for ODEs were first introduced in [10] and have been subsequently refined and extended in [5, 13, 15, 21, 24, 25]. SDC methods construct high-order solutions within one time step by iteratively approximating a series of correction equations at collocation nodes using low-order sub-stepping methods.

Consider the generic ODE initial value problem

$$u'(t) = f(u(t), t), \quad u(0) = u_0 \quad (12)$$

where  $t \in [0, T]$ ;  $u_0, u(t) \in \mathbb{C}^N$ ; and  $f : \mathbb{R} \times \mathbb{C}^N \rightarrow \mathbb{C}^N$ . SDC methods are derived by considering the equivalent Picard integral form of (12) given by

$$u(t) = u_0 + \int_0^t f(u(s), s) ds. \quad (13)$$

A single time step  $[t_n, t_{n+1}]$  is divided into a set of intermediate sub-steps by defining  $M + 1$  collocation points  $\tau_m \in [t_n, t_{n+1}]$  such that  $t_n = \tau_0 < \tau_1 < \dots < \tau_M = t_{n+1}$ . Then, the integrals of  $f(u(t), t)$  over each of the intervals  $[t_n, \tau_m]$  are approximated by

$$I_n^m \equiv \int_{t_n}^{\tau_m} f(u(s), s) ds \approx \Delta t \sum_{j=0}^M q_{mj} f(U_j, \tau_j) \quad (14)$$

where  $U_j \approx u(\tau_j)$ ,  $\Delta t = t_{n+1} - t_n$ , and  $q_{mj}$  are quadrature weights. The quadrature weights that give the highest order of accuracy given the collocation points  $\tau_m$  are obtained by computing exact integrals of the Lagrange interpolating polynomial over the collocation points  $\tau_m$ . Note that each of the integral approximations  $I_n^m$  (that represent the integral of  $f$  from  $t_n$  to  $\tau_m$ ) in (14) depends on the function values  $f(U_m, \tau_m)$  at all of the collocation nodes  $\tau_m$ .

To simplify notation, we define the *integration matrix*  $\mathbf{Q}$  to be the  $M \times (M + 1)$  matrix consisting of entries  $q_{mj}$ ; and the vectors  $\mathbf{U} \equiv [U_1, \dots, U_M]$  and  $\mathbf{F} \equiv [f(U_0, t_0), \dots, f(U_M, t_M)]$ . With these definitions, the Picard equation (13) within the time step  $[t_n, t_{n+1}]$  is approximated by

$$\mathbf{U} = \mathbf{U}_0 + \Delta t \mathbf{Q} \mathbf{F} \quad (15)$$

where  $U_0 = U_0 \mathbf{1}$ . Note again that the integration matrix  $Q$  is dense so that each entry of  $U$  depends on all other entries of  $U$  (through  $F$ ) and  $U_0$ . Thus, (15) is an implicit equation for the unknowns in  $U$  at all of the quadrature points. Finally, we note that the solution of (15) corresponds to the collocation or implicit Runge-Kutta solution of (12) over the nodes  $\tau_m$ . Hence SDC can be considered as an iterative method for solving the spectral collocation formulation.

The SDC scheme used here begins by spreading the initial condition  $u_n$  to each of the collocation nodes so that the provisional solution  $U^0$  is given by  $U^0 = [U_0, \dots, U_0]$ . Subsequent iterations (denoted by  $k$  superscripts) proceed by applying the *node-to-node integration matrix*  $S$  to  $F^k$  and correcting the result using a forward-Euler time-stepper between the collocation nodes. The node-to-node integration matrix  $S$  is used to approximate the integrals  $I_m^{m+1} = \int_{\tau_m}^{\tau_{m+1}} f(u(s), s) ds$  (as opposed to the integration matrix  $Q$  which approximates  $I_n^m$ ) and is constructed in a manner similar to the integration matrix  $Q$ . The update equation corresponding to the forward-Euler sub-stepping method for computing  $U^{k+1}$  is given by

$$U_{m+1}^{k+1} = U_m^{k+1} + \Delta t_m [f(U_m^{k+1}, t_m) - f(U_m^k, t_m)] + \Delta t S^{k,m} \quad (16)$$

where  $S^{k,m}$  is the  $m^{\text{th}}$  row of  $SF^k$ . The process of computing (16) at all of the collocation nodes  $\tau_m$  is referred to as an *SDC sweep* or an *SDC iteration*. The accuracy of the solution generated after  $k$  SDC iterations done with such a first-order method is formally  $O(\Delta t^k)$  as long as the spectral integration rule (which is determined by the choice of collocation nodes  $\tau_m$ ) is at least order  $k$ .

In the examples presented in §5, a method of lines discretization based on the spatial discretization presented in §2 is used to reduce the partial differential equations (PDEs) in question to a large system of ODEs.

The computational cost of the SDC scheme used here is determined by the number of nodes  $M+1$  chosen and the number of SDC iterations  $K$  taken per time step. The number of resulting function evaluations  $N_{\text{evals}}$  is  $N_{\text{evals}} = KM$ . For example, with 3 Gauss-Lobatto ( $M = 2$ ) nodes, the resulting integration rule is 4<sup>th</sup> order. To achieve this formal order of accuracy we perform  $K = 4$  SDC iterations per time step and hence we require  $N_{\text{evals}} = 8$  function evaluations (note that  $F(U_0, 0)$  is recycled from the previous time step, and hence the first time-step requires 9 function evaluations).

By increasing the number of SDC nodes and adjusting the number of SDC iterations taken, we can construct schemes of arbitrary order. For example, to construct a 6<sup>th</sup> order scheme one could use a 5 point Gauss-Lobatto integration rule (which is 8<sup>th</sup> order accurate), but only take 6 SDC iterations. For high order explicit schemes used here we have observed that the SDC iterations sometimes converge to the collocation solution in fewer iterations than is formally required. This can be detected by computing the SDC residual

$$R^k = U_0 + \mathbf{q} \cdot F^k - U_M^k, \quad (17)$$

where  $\mathbf{q}$  is the last row of  $Q$ , and comparing successive residuals. If  $|R^{k-1}|/|R^k|$  is close to one, the SDC iterations have converged to the collocation solution and subsequent iterations can be skipped.

### 3.2 Multirate Integration

Multirate SDC (MRSDC) methods use a hierarchy of SDC schemes to integrate systems that contain processes with disparate time-scales more efficiently than



fully coupled methods [5, 21]. A traditional MRSDC method integrates processes with long time-scales with fewer SDC nodes than those with short time-scales. They are similar in spirit to sub-cycling schemes in which processes with short characteristic time-scales are integrated with smaller time steps than those with long characteristic time-scales. MRSDC schemes, however, update the short time-scale components of the solutions at the long time-scale time steps during each MRSDC iteration, as opposed to only once for typical sub-cycling schemes, which results in tighter coupling between processes throughout each time-step [5, 21].

Before presenting MRSDC in detail, we note that the primary advantage of MRSDC schemes lies in how the processes are coupled. For systems in which the short time-scale process is moderately stiff, using more SDC nodes than the long time-scale process helps alleviate the stiffness of the short time-scale processes. However, extremely stiff processes are best integrated between SDC nodes with, for example, a variable order/step-size backward differentiation formula (BDF) scheme. In this case, the short time-scale processes can in fact be treated with fewer SDC nodes than long time-scale processes.

Consider the generic ODE initial value problem with two disparate time-scales

$$u'(t) = f_1(u(t), t) + f_2(u(t), t), \quad u(0) = u_0 \quad (18)$$

where we have split the generic right-hand-side  $f$  in (12) into two components:  $f_1$  and  $f_2$ . A single time step  $[t_n, t_{n+1}]$  is first divided into a set of intermediate sub-steps by defining  $M_1 + 1$  collocation points such that  $\tau_m \in [t_n, t_{n+1}]$ . The vector of these  $M_1 + 1$  collocation points  $\tau_m$  is denoted  $\mathbf{t}_1$ , and these collocation points will be used to integrate the  $f_1$  component. The time step is further divided by defining  $M_2 + 1$  collocation points  $\tau_p \in [t_n, t_{n+1}]$  such that  $\mathbf{t}_1 \subset \mathbf{t}_2$ , where  $\mathbf{t}_2$  is the vector of these new  $\tau_p$  collocation points. These collocation points will be used to integrate the  $f_2$  component. That is, a hierarchy of collocation points is created with  $\mathbf{t}_1 \subset \dots \subset \mathbf{t}_N$ . The splitting of the right-hand-side in (18) should be informed by the numerics at hand. Traditionally, slow time-scale processes are split into  $f_1$  and placed on the  $\mathbf{t}_1$  nodes, and fast time-scale processes are split into  $f_2$  and placed on the  $\mathbf{t}_2$  nodes. However, if the algorithm used to evolve the fast time-scale process in the MRSDC update equation (21) is less stiff than the algorithm for the slow time-scale process, then the roles of the processes within MRSDC can be swapped. As such, we hereafter refer to the collocation points in  $\mathbf{t}_1$  as the “coarse nodes” and those in  $\mathbf{t}_2$  as the “fine nodes”.

The SDC nodes  $\mathbf{t}_1$  for the coarse component are typically chosen to correspond to a formal quadrature rule like the Gauss-Lobatto rule. These nodes determine the overall order of accuracy of the resulting MRSDC scheme. Subsequently, there is some flexibility in how the nodes for fine components are chosen. For example, the points in  $\mathbf{t}_2$  can be chosen to correspond to a formal quadrature rule

- (a) over the entire time step  $[t_n, t_{n+1}]$ ;
- (b) over each of the intervals defined by the points in  $\mathbf{t}_1$ ;
- (c) over several sub-intervals of the intervals defined by the points in  $\mathbf{t}_1$ ;

Note that in the first case, a quadrature rule that nests (or embeds) itself naturally is required (such as the Clenshaw-Curtis rule), whereas in the second and third cases the nodes in  $\mathbf{t}_2$  usually do not correspond to a formal quadrature rule over the entire time step  $[t_n, t_{n+1}]$ . In the second and third cases we note that the basis used to construct the  $\mathbf{Q}$  and  $\mathbf{S}$  integration matrices are typically piecewise polynomial – this allows us to shrink the effective time-step size of the fine process without constructing an excessively high-order polynomial interpolant. These three

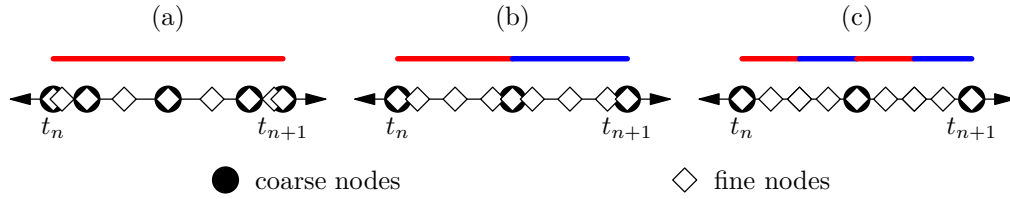


Figure 1. MRSDC quadrature nodes. (a) The left axis shows an MRSDC hierarchy with  $t_1$  corresponding to 5 Clenshaw-Curtis nodes and  $t_2$  corresponding to 9 Clenshaw-Curtis nodes. (b) The middle axis shows an MRSDC hierarchy with  $t_1$  corresponding to 3 Gauss-Lobatto nodes and  $t_2$  corresponding to 5 Gauss-Lobatto nodes between each pair of nodes in  $t_1$ . (c) The right axis shows an MRSDC hierarchy with  $t_1$  corresponding to 3 Gauss-Lobatto nodes and  $t_2$  corresponding to 3 Gauss-Lobatto nodes repeated twice between each pair of nodes in  $t_1$ . The red and blue lines show that the MRSDC integration matrix  $\mathbf{Q}_{2,2}$  is constructed with (a) one polynomial spanning all 9 fine nodes, (b) two polynomials spanning 5 fine nodes each, and (c) four polynomials spanning 3 fine nodes each.

possibilities are depicted in Fig. 1.

Once the SDC nodes for the desired MRSDC scheme have been chosen, the node-to-node and regular integration matrices ( $\mathbf{S}$  and  $\mathbf{Q}$ , respectively) can be constructed. While single-rate SDC schemes, as presented in §3.1, require one set of  $\mathbf{S}$  and  $\mathbf{Q}$  matrices, the two-component MRSDC scheme used here requires two sets of  $\mathbf{S}$  and  $\mathbf{Q}$  matrices. These are denoted with subscripts  $i, j$  so that the action of  $\mathbf{S}_{i,j}$  approximates the node-to-node integrals between nodes in  $t_i$  of the  $\mathbf{F}_j$  component that “lives” on the  $t_j$  nodes, and similarly for the  $\mathbf{Q}_{i,j}$  matrices. Note that both  $\mathbf{S}_{i,j}$  and  $\mathbf{Q}_{i,j}$  are of size  $M_i \times (M_j + 1)$ .

With these definitions, the Picard equation (13) within the time step  $[t_n, t_{n+1}]$  is approximated by

$$\mathbf{U} = \mathbf{U}_0 + \Delta t \mathbf{Q}_{2,1} \mathbf{F}_1 + \Delta t \mathbf{Q}_{2,2} \mathbf{F}_2 \quad (19)$$

where  $\mathbf{U}$  is the vector of approximate solution values  $U_q$  over the fine nodes in  $t_2$ . The MRSDC scheme used in SMC has two operating modes:

- (1) The coarse ( $f_1$ ) and fine ( $f_2$ ) components of (18) correspond to the advection-diffusion and reaction parts of (1), respectively, and the forward-Euler sub-stepping scheme is used for both components.
- (2) The coarse ( $f_1$ ) and fine ( $f_2$ ) components of (18) correspond to the reaction and advection-diffusion parts of (1), respectively. The advection-diffusion component is treated with a forward-Euler sub-stepper while the reaction component is treated with the variable-order BDF scheme in VODE [6].

In the first mode, the scheme is purely explicit whereas in the second mode the algorithm uses an implicit treatment of reactions. Which version is most appropriate for a given simulation depends on the relative stiffness of chemistry and fluid dynamics. When the chemical time scales are not significantly disparate from the fluid mechanical time scale, the fully explicit version will be the most efficient. When the chemistry is extremely stiff, the second mode is preferred.

The MRSDC update equation used in SMC for mode 1 over the nodes in  $t_2$  is given by

$$\begin{aligned} U_{q+1}^{k+1} = & U_q^{k+1} + \Delta t_q [f_1(U_p^{k+1}, t_p) - f_1(U_p^k, t_p)] \\ & + \Delta t_q [f_2(U_q^{k+1}, t_q) - f_2(U_q^k, t_q)] + \Delta t S_{2,2}^{k,q} + \Delta t S_{2,1}^{k,q} \end{aligned} \quad (20)$$

where  $S_{2,j}^{k,q}$  is the  $q^{\text{th}}$  row of  $\mathbf{S}_{2,j} \mathbf{F}_j$ , and the  $p^{\text{th}}$  node of the fine component corresponds to the closest coarse node to the left of the fine node  $q$ . That is, the coarse component  $f_1$  is held constant, and equal to its value at the left coarse node

$p = \lfloor q/(M_2/M_1) \rfloor$ , during the fine updating steps. The update equation for mode 2 is

$$\begin{aligned} U_{q+1}^{k+1} = & U_q^{k+1} + \Delta t_q [f_1(U_{p+1}^{k+1}, t_p) - f_1(U_{p+1}^k, t_p)] \\ & + \Delta t_q [f_2(U_q^{k+1}, t_q) - f_2(U_q^k, t_q)] + \Delta t S_{2,2}^{k,q} + \Delta t S_{2,1}^{k,q} \end{aligned} \quad (21)$$

where  $f_1(U_{p+1}^{k+1}, t_p)$  is computed with VODE.

The computational cost of an MRSDC scheme is determined by the number of nodes  $M_\ell + 1$  chosen for each multirate component  $\ell$  and the number of SDC iterations  $K$  taken per time step. The number of resulting function evaluations  $N_{\text{evals}}^\ell$  per component  $\ell$  is  $N_{\text{evals}}^\ell = KM_\ell$ . For example, with 3 Gauss-Lobatto ( $M = 2$ ) nodes for the coarse component and 5 Gauss-Lobatto nodes for the fine component between each of the coarse nodes (so that there are 9 nodes in  $t_2$  and hence  $M_2 = 8$ ), the number of coarse function evaluations over  $K = 4$  iterations is  $N_{\text{evals}}^1 = 8$ , and the number of fine function evaluations is  $N_{\text{evals}}^2 = 32$ .

The reacting compressible Navier-Stokes equations (1) have two characteristic time-scales: one over which advection and diffusion processes evolve, and another over which reactions evolve. The reaction time-scale is usually shorter than the advection/diffusion time-scale. As such, the coarse and fine MRSDC nodes typically correspond to the advection/diffusion and reaction parts of (1), respectively. However, as is the case for the Dimethyl Ether Jet problem shown in §5.3, the reaction terms in (1) can become so stiff that it becomes impractical to integrate them explicitly. In these cases, SMC employs the variable-order BDF schemes in VODE [6] to integrate the reaction terms semi-implicitly. This effectively reverses the time-step constraint of the system: the reaction terms can be integrated using VODE (which internally takes many steps) with a larger time-step than the advection-diffusion terms. As such, the roles of the coarse and fine MRSDC nodes can be reversed so that the coarse and fine MRSDC nodes correspond to the reaction and advection-diffusion terms of (1), respectively.

#### 4. Parallelization

SMC is implemented within the BoxLib software framework with a hybrid MPI-OpenMP approach for parallelization [1]. In BoxLib, the computational domain is divided into boxes. Each MPI process owns one or more boxes via decomposition of the spatial domain and it can spawn multiple OpenMP threads. For parallelization with OpenMP, the traditional approach is a fine-grained approach in which individual loops are threaded using OpenMP PARALLEL DO directives (with COLLAPSE clause if the number of threads is relatively large). This approach works well for tasks like computing transport coefficients and chemistry production rates because there is only one PARALLEL DO region for each box. However, the fine-grained parallelism approach does not work well for computing diffusive and hyperbolic terms. The reason for this is that many loops are used in computing terms like  $\nabla \cdot \mathcal{F}_k$ . This results in many PARALLEL DO regions with serial parts in between that, in turn, can incur significant overheads and limit parallel efficiency. To overcome these issues in the fine-grained parallelism approach, a coarse-grained approach is taken for computing diffusive and hyperbolic terms. In our coarse-grained parallelism approach, OpenMP PARALLEL DO directives are not used. Instead, a SPMD (single program, multiple data) style is used. Each thread works on its own domain. Listing 1 shows a code snippet illustrating the coarse-grained parallelism approach. Here `q`, `coe` and `dUdt` are four-dimensional

Fortran arrays for primitive variables, transport coefficients, and rate of change of conserved variables, respectively. These shared arrays contain data for the entire box. The `get_threadbox` subroutine computes the bounds of sub-boxes owned by each thread and stores them in private arrays `lo` and `hi`. The original box (without ghost cells) is entirely covered by the sub-boxes without overlap. Typically, the domain decomposition among threads is performed in  $y$  and  $z$ -dimensions, but not in  $x$ -dimension, because the  $x$ -dimension of our data arrays is contiguous in memory. The `diffterm` subroutine is called by each thread with private `lo` and `hi`, and it has local variables (including arrays) that are automatically private to each thread. Note that there are no OpenMP statements in the `diffterm` subroutine. This makes it easy to avoid OpenMP related bugs.

Listing 1 Fortran code snippet illustrating the coarse-grained parallelism approach.

---

```

subroutine compute_dUdt() ! for a box of nx * ny * nz cells
! Only part of the subroutine is shown here
integer :: lo(3), hi(3)
!$omp parallel private(lo,hi)
call get_threadbox(lo,hi)
call diffterm(lo,hi,q,coe,dUdt)
!$omp end parallel
end subroutine compute_dUdt

subroutine diffterm(lo,hi,q,coe,dUdt)
! Only part of the subroutine is shown here
integer, intent(in) :: lo(3), hi(3)
! q and coe have four ghost cells in each side
real, intent(in) :: q(-3:nx+4,-3:ny+4,-3:nz+4,nq)
real, intent(in) :: coe(-3:nx+4,-3:ny+4,-3:nz+4,nc)
real, intent(inout) :: dUdt( 1:nx , 1:ny , 1:nz , nu)
! tmp is a local array
real :: tmp(lo(1)-4:hi(1)+4,lo(2)-4:hi(2)+4,lo(3)-4:hi(3)+4)
! a nested loop
! In the fine-grained approach, this line would be !$omp do.
do k =lo(3)-4,hi(3)+4
do j =lo(2)-4,hi(2)+4
do i=lo(1)-4,hi(1)+4
tmp(i,j,k) = .....
end do
end do
end do
! another nested loop
! In the fine-grained approach, this line would be !$omp do.
do k =lo(3),hi(3)
do j =lo(2),hi(2)
do i=lo(1),hi(1)
dUdt(i,j,k,1) = .....
end do
end do
end do
end subroutine diffterm

```

---

## 5. Numerical Results

In this section we present numerical tests to demonstrate the designed convergence rate and performance of SMC. We also compare simulation results obtained using SMC with the results from the low Mach number LMC code [4, 9, 26]. Numerical simulations presented here use EGLIB [11, 12] to compute transport coefficients.

## 5.1 Convergence

### 5.1.1 Space/time Convergence

In this section we present numerical tests to demonstrate the designed convergence rate of SMC for the single-rate SDC integrator.

The convergence tests presented here are set up as follows. The simulations use a 9-species  $\text{H}_2/\text{O}_2$  reaction mechanism [23]. The computational domain is  $L_x = L_y = L_z = (-0.0005 \text{ m}, 0.0005 \text{ m})$  with periodic boundaries in all three dimensions. The initial pressure, temperature and velocity of the gas are set to

$$p = p_0 \left[ 1 + 0.1 \exp \left( -\frac{r^2}{r_0^2} \right) \right], \quad (22)$$

$$T = T_0 + T_1 \exp \left( -\frac{r^2}{r_0^2} \right), \quad (23)$$

$$v_x = v_0 \sin \left( \frac{2\pi}{L_x} x \right) \cos \left( \frac{2\pi}{L_y} y \right) \cos \left( \frac{2\pi}{L_z} z \right), \quad (24)$$

$$v_y = -v_0 \cos \left( \frac{2\pi}{L_x} x \right) \sin \left( \frac{2\pi}{L_y} y \right) \cos \left( \frac{2\pi}{L_z} z \right), \quad (25)$$

$$v_z = 0, \quad (26)$$

where  $p_0 = 1 \text{ atm}$ ,  $T_0 = 300 \text{ K}$ ,  $T_1 = 1100 \text{ K}$ ,  $v_0 = 3 \text{ m s}^{-1}$ ,  $r_0 = 0.0001 \text{ m}$ , and  $r = \sqrt{x^2 + y^2 + z^2}$ . The mole fractions of species are initially set to zero except that

$$X(\text{H}_2) = 0.1 + 0.025 \exp \left( -\frac{r^2}{r_0^2} \right), \quad (27)$$

$$X(\text{O}_2) = 0.25 + 0.050 \exp \left( -\frac{r^2}{r_0^2} \right), \quad (28)$$

$$X(\text{N}_2) = 1 - X(\text{H}_2) - X(\text{O}_2). \quad (29)$$

To demonstrate convergence, we performed a series of runs with increasing spatial and temporal resolutions. A single-rate SDC scheme with 5 Gauss-Lobatto nodes and 8 SDC iterations is used for time stepping. The simulations are stopped at  $t = 8 \times 10^{-7} \text{ s}$ . When the spatial resolution changes by a factor of 2 from one run to another, we also change the time step by a factor of 2. Therefore, the convergence rate in this study is expected to be 8<sup>th</sup> order. Table 1 shows the  $L_0$  and  $L_2$ -norm errors and convergence rates for  $\rho$ ,  $T$ ,  $\mathbf{u}$ ,  $Y(\text{H}_2)$ ,  $Y(\text{O}_2)$ ,  $Y(\text{OH})$ ,  $Y(\text{H}_2\text{O})$ , and  $Y(\text{N}_2)$ . Because there is no analytic solution for this problem, we compute the errors by comparing the numerical solution using  $N^3$  points with the solution using  $(2N)^3$  points. The  $L_2$ -norm error is computed as

$$L_2(N) = \sqrt{\frac{1}{N^3} \sum_{i=1}^N \sum_{j=1}^N \sum_{k=1}^N (\phi_{N,ijk} - \phi_{2N,ijk})^2}, \quad (30)$$

where  $\phi_{N,ijk}$  is the solution at point  $(i, j, k)$  of the  $N^3$  point run and  $\phi_{2N,ijk}$  is the solution of the  $(2N)^3$  point run at the same location. It is often difficult to obtain high-order convergence rates in direct three-dimensional numerical simula-

tions with complex chemistry and detailed transport – the resolution must be high enough that the numerical solutions are in the regime of asymptotic convergence. On the other hand, numerical solutions are subject to round-off errors, which can become a significant source of errors for high-resolution solutions. Nevertheless, the results of our simulations demonstrate the high-order convergence rate of our scheme. The  $L_0$  and  $L_2$ -norm convergence rates for various variables in the simulations approach 8<sup>th</sup> order, the designed order of the scheme. Relatively low orders ( $\sim 3-4$ ) are observed in the  $L_0$ -norm convergence rate of  $Y(\text{H}_2)$ ,  $Y(\text{O}_2)$  and  $Y(\text{N}_2)$  for the  $256^3$  point run. Given that (1) high orders are obtained for the  $L_2$ -norm convergence rate of these three variables in the  $256^3$  point run; (2) high orders are obtained for the  $L_0$ -norm convergence rate of these variables in lower resolution runs; (3) high orders (close to 8) are obtained in the mass fraction of trace species such as  $Y(\text{OH})$  for both  $L_0$  and  $L_2$ -norm convergence rates; and (4) these three species are the dominant species with high mass fractions, it is thus reasonable to attribute the degradation in  $L_0$ -norm convergence rate to round-off errors.

### 5.1.2 Multirate Integration

In this section we present numerical tests to demonstrate the designed convergence rate of the MRSDC integrator in SMC.

Table 2 shows the  $L_0$  and  $L_2$ -norm errors and convergence rates for  $\rho$ ,  $T$ ,  $u_x$ ,  $Y(\text{H}_2)$ ,  $Y(\text{O}_2)$ ,  $Y(\text{OH})$ ,  $Y(\text{H}_2\text{O})$ , and  $Y(\text{N}_2)$  for the same test problem as described in §5.1. All runs were performed on a  $32^3$  grid, so that the errors and convergence rates reported here are ODE errors. Because there is no analytic solution for this problem, a reference solution was computed using the same spatial grid, but with an 8<sup>th</sup>-order single-rate SDC integrator and  $\Delta t = 1.25 \times 10^{-9}$ s. We note that the  $L_0$  and  $L_2$ -norm convergence rates for all variables and MRSDC configurations are 4<sup>th</sup>-order, as expected since the coarse MRSDC component uses 3 Gauss-Lobatto nodes. This verifies that the MRSDC implementation in SMC operates according to its specifications regardless of how the fine nodes are chosen (see §3.2).

## 5.2 Performance

### 5.2.1 Parallel Performance

In this section we present numerical tests to demonstrate the parallel efficiency of SMC.

A strong scaling study was carried out on a 61-core 1.1 GHz Intel Xeon Phi coprocessor that supported up to 244 hyperthreads. We performed a series of pure OpenMP runs, each consisting of a single box of  $128^3$  points, of the test problem in section 5.1 using various number of threads. The simulations are run for 10 time steps. Table 3 shows that SMC has excellent thread scaling behavior. An 86 times speedup over the 1 thread run is obtained on the 61-core coprocessor using 240 hyperthreads.

We also performed a weak scaling study using the test problem in section 5.1 on the Hopper supercomputer at the National Energy Research Scientific Computing Center. Each compute node of Hopper has 4 non-uniform memory access (NUMA) nodes, with 6 cores on each NUMA node. In this weak scaling study, a hybrid MPI/OpenMP approach with 6 threads per MPI process is used. Each MPI process works on two  $64^3$  point boxes. The simulations are run for 10 time steps. Table 4 shows the average wall clock time per time step for a series of runs on various number of cores. We use the 6-core run as baseline and define parallel efficiency for an  $n$ -core run as  $T_6/T_n$ , where  $T_6$  and  $T_n$  are the average wall clock time per time step for the 6 and  $n$ -core runs, respectively. Excellent scaling to about 100

Table 1. Errors and convergence rates for three-dimensional simulations of a hydrogen flame using single-rate SDC and 8<sup>th</sup> order finite difference stencil. Density  $\rho$ , temperature  $T$  and  $\mathbf{u}$  are in SI units.

Variable	No. of Points	$\Delta t$ ( $10^{-9}$ s)	$L_0$ Error	$L_0$ Rate	$L_2$ Error	$L_2$ Rate
$\rho$	32 <sup>3</sup>	4	1.992E-03		2.848E-04	
	64 <sup>3</sup>	2	1.219E-04	4.03	1.748E-05	4.03
	128 <sup>3</sup>	1	3.175E-06	5.26	2.784E-07	5.97
	256 <sup>3</sup>	0.5	2.731E-08	6.86	1.688E-09	7.37
$T$	32 <sup>3</sup>	4	3.171E-01		3.676E-02	
	64 <sup>3</sup>	2	1.364E-02	4.54	1.992E-03	4.21
	128 <sup>3</sup>	1	3.536E-04	5.27	3.102E-05	6.01
	256 <sup>3</sup>	0.5	9.535E-06	5.21	1.912E-07	7.34
$u_x$	32 <sup>3</sup>	4	4.522E-01		5.923E-02	
	64 <sup>3</sup>	2	4.088E-02	3.47	3.377E-03	4.13
	128 <sup>3</sup>	1	1.025E-03	5.32	5.275E-05	6.00
	256 <sup>3</sup>	0.5	8.533E-06	6.91	3.185E-07	7.37
$u_y$	32 <sup>3</sup>	4	4.567E-01		6.088E-02	
	64 <sup>3</sup>	2	3.664E-02	3.64	3.519E-03	4.11
	128 <sup>3</sup>	1	1.065E-03	5.10	5.574E-05	5.98
	256 <sup>3</sup>	0.5	9.202E-06	6.85	3.389E-07	7.36
$u_z$	32 <sup>3</sup>	4	4.335E-01		6.004E-02	
	64 <sup>3</sup>	2	3.974E-02	3.45	3.447E-03	4.12
	128 <sup>3</sup>	1	9.962E-04	5.32	5.422E-05	5.99
	256 <sup>3</sup>	0.5	8.603E-06	6.86	3.285E-07	7.37
$Y(\text{H}_2)$	32 <sup>3</sup>	4	2.406E-06		1.025E-07	
	64 <sup>3</sup>	2	1.575E-07	3.93	5.560E-09	4.20
	128 <sup>3</sup>	1	1.199E-09	7.04	1.037E-10	5.74
	256 <sup>3</sup>	0.5	6.300E-11	4.25	7.404E-13	7.13
$Y(\text{O}_2)$	32 <sup>3</sup>	4	1.988E-05		8.302E-07	
	64 <sup>3</sup>	2	2.659E-07	6.22	1.054E-08	6.30
	128 <sup>3</sup>	1	1.613E-09	7.36	1.405E-10	6.23
	256 <sup>3</sup>	0.5	1.225E-10	3.72	1.012E-12	7.12
$Y(\text{OH})$	32 <sup>3</sup>	4	3.464E-12		2.386E-14	
	64 <sup>3</sup>	2	3.299E-14	6.71	1.738E-16	7.10
	128 <sup>3</sup>	1	2.073E-16	7.31	1.049E-18	7.37
	256 <sup>3</sup>	0.5	9.357E-19	7.79	4.661E-21	7.81
$Y(\text{H}_2\text{O})$	32 <sup>3</sup>	4	7.493E-12		5.009E-14	
	64 <sup>3</sup>	2	6.509E-14	6.85	3.560E-16	7.14
	128 <sup>3</sup>	1	3.963E-16	7.36	2.141E-18	7.38
	256 <sup>3</sup>	0.5	1.765E-18	7.81	9.457E-21	7.82
$Y(\text{N}_2)$	32 <sup>3</sup>	4	1.758E-05		7.910E-07	
	64 <sup>3</sup>	2	1.894E-07	6.54	7.294E-09	6.76
	128 <sup>3</sup>	1	5.686E-10	8.38	3.994E-11	7.51
	256 <sup>3</sup>	0.5	7.089E-11	3.00	3.108E-13	7.01

thousand cores is observed.

### 5.2.2 Multirate Integration

Table 5 compares run time and function evaluation counts for various configurations of the SDC and MRSDC integrators used in SMC for a premixed methane flame contained in a cubic box ( $L_x = L_y = L_z = 0.008\text{m}$ ) with periodic boundary conditions in the  $x$  and  $y$  directions, and inlet/outlet boundary conditions in the  $z$  direction. The GRI-MECH 3.0 chemistry network (53 species, 325 reactions) [32] was used so that the reaction terms in (1) were quite stiff and an MRSDC integrator with the reaction terms on the fine nodes was appropriate. A reference solution was computed using a single-rate SDC integrator with a time step  $\Delta t$  of

Table 2. Errors and convergence rates for three-dimensional simulations of a hydrogen flame using 4<sup>th</sup> order MRSDC and 8<sup>th</sup> order finite difference stencil. Density  $\rho$ , temperature  $T$  and  $\mathbf{u}$  are in SI units. The MRSDC  $X / Y$  configurations use  $X$  coarse nodes and  $Y$  fine nodes between each pair of coarse nodes (type (b) in §3.2). The MRSDC  $X / Y \times R$  configurations use  $X$  coarse nodes and  $Y$  fine nodes repeated  $R$  times between each pair of coarse nodes (type (c) in §3.2). All SDC nodes are Gauss-Lobatto (GL) nodes. Density  $\rho$ , temperature  $T$  and  $\mathbf{u}$  are in SI units.

SDC Configuration	Variable	$\Delta t (10^{-9} \text{ s})$	$L_0$ Error	$L_0$ Rate	$L_2$ Error	$L_2$ Rate	
GL 3 / GL 9	$\rho$	10	5.638e-07		3.958e-08		
		5	3.392e-08	4.06	2.426e-09	4.03	
		2.5	2.093e-09	4.02	1.509e-10	4.01	
	$T$	10	2.748e-04		1.577e-05		
		5	1.661e-05	4.05	9.504e-07	4.05	
		2.5	1.029e-06	4.01	5.877e-08	4.02	
	$u_x$	10	6.928e-04		2.253e-05		
		5	4.255e-05	4.03	1.369e-06	4.04	
		2.5	2.650e-06	4.01	8.496e-08	4.01	
	$Y(\text{H}_2)$	10	1.960e-09		5.051e-11		
		5	1.160e-10	4.08	3.059e-12	4.05	
		2.5	7.108e-12	4.03	1.896e-13	4.01	
	$Y(\text{O}_2)$	10	9.501e-09		3.340e-10		
		5	5.762e-10	4.04	2.027e-11	4.04	
		2.5	3.562e-11	4.02	1.255e-12	4.01	
	$Y(\text{OH})$	10	5.989e-17		3.531e-19		
		5	3.671e-18	4.03	2.183e-20	4.02	
		2.5	2.292e-19	4.00	1.370e-21	3.99	
	$Y(\text{H}_2\text{O})$	10	4.309e-18		6.660e-20		
		5	2.519e-19	4.10	3.928e-21	4.08	
		2.5	1.527e-20	4.04	2.394e-22	4.04	
	$Y(\text{N}_2)$	10	8.743e-09		3.191e-10		
		5	5.258e-10	4.06	1.938e-11	4.04	
		2.5	3.238e-11	4.02	1.200e-12	4.01	
	GL 3 / GL $5 \times 2$	$\rho$	10	5.638e-07		3.958e-08	
			5	3.392e-08	4.06	2.426e-09	4.03
			2.5	2.093e-09	4.02	1.509e-10	4.01
$T$		10	2.748e-04		1.577e-05		
		5	1.661e-05	4.05	9.504e-07	4.05	
		2.5	1.029e-06	4.01	5.877e-08	4.02	
$u_x$		10	6.928e-04		2.253e-05		
		5	4.255e-05	4.03	1.369e-06	4.04	
		2.5	2.650e-06	4.01	8.496e-08	4.01	
$Y(\text{H}_2)$		10	1.960e-09		5.051e-11		
		5	1.160e-10	4.08	3.059e-12	4.05	
		2.5	7.108e-12	4.03	1.896e-13	4.01	
$Y(\text{O}_2)$		10	9.501e-09		3.340e-10		
		5	5.762e-10	4.04	2.027e-11	4.04	
		2.5	3.562e-11	4.02	1.255e-12	4.01	
$Y(\text{OH})$		10	5.989e-17		3.531e-19		
		5	3.671e-18	4.03	2.183e-20	4.02	
		2.5	2.292e-19	4.00	1.370e-21	3.99	
$Y(\text{H}_2\text{O})$		10	4.309e-18		6.660e-20		
		5	2.519e-19	4.10	3.928e-21	4.08	
		2.5	1.527e-20	4.04	2.394e-22	4.04	
$Y(\text{N}_2)$		10	8.743e-09		3.191e-10		
		5	5.258e-10	4.06	1.938e-11	4.04	
		2.5	3.238e-11	4.02	1.200e-12	4.01	



Table 3. Strong scaling behavior of pure OpenMP runs on a 61-core Intel Xeon Phi coprocessor. Average wall clock time per time step and speedup are shown for runs using various number of threads. Hyperthreading is used for the 128 and 240-thread runs.

No. of Threads	Wall Time per Step (s)	Speedup
1	1223.58	
2	626.13	2.0
4	328.97	3.7
8	159.88	7.7
16	79.73	16
32	40.12	31
60	24.55	50
128	18.19	67
240	14.28	86

Table 4. Weak scaling behavior of hybrid MPI/OpenMP runs on Hopper at NERSC. Average wall clock time per time step and parallel efficiency are shown for runs on various number of cores. Each MPI process spawns 6 OpenMP threads.

No. of Cores	No. of MPI Processes	Wall Time per Step (s)	Parallel Efficiency
6	1	13.72	
24	4	14.32	96%
192	32	14.46	95%
1536	256	14.47	95%
12288	2048	15.02	91%
98304	16384	15.32	90%

$1 \times 10^{-9}$ s to a final time of  $4.2 \times 10^{-7}$ s. All simulations were run on a  $32^3$  point grid. For each integrator, the test was run using successively larger time steps until the SDC integrator failed to converge. The largest time step that matched the reference solution (to within a relative  $L_0$  error of less than  $1 \times 10^{-5}$ ) is reported. All integrators use 3 Gauss-Lobatto nodes for the coarse component and hence all integrators are formally 4<sup>th</sup> order accurate. We note that all of the multi-rate integrators are able to use larger time steps than the single-rate integrator due to the stiffness of the reaction terms: the multi-rate integrators use more nodes to integrate the reaction terms and hence the effective time-steps used in the update equation (21) are smaller. This means that, in all cases, the multi-rate integrators evaluate the advection/diffusion terms less frequently than the single-rate integrator. However, in all but one case, the multi-rate integrators also evaluate the reaction terms more frequently than the single-rate integrator. The trade-off between the frequency of evaluating the advection/diffusion vs reaction terms is highlighted by comparing the MRSDC 3 GL / 9 GL and MRSDC 3 GL / 13 GL runs: the run with 13 fine nodes can use a slightly larger time-step at the cost of evaluating the reaction terms more frequently, resulting in only a very slight runtime advantage over the run using 9 fine nodes and a smaller time-step. Ultimately the largest runtime advantage is realized by choosing a multi-rate configuration that allows a large time-step to be taken without requiring too many extra calls to the reaction network. For this test the MRSDC 3 /  $5 \times 2$  configuration achieves this goal and is able to run to completion approximately 6.0 times faster than the single-rate SDC integrator.

### 5.3 Dimethyl Ether Jet

We present here a two-dimensional simulation of jet using a 39-species dimethyl ether (DME) chemistry mechanism [2]. A 2D Cartesian domain,  $-0.00114 \text{ m} < x < 0.00114 \text{ m}$  and  $0 < y < 0.00228 \text{ m}$ , is used for this test. Pressure is initially set to

Table 5. Comparison of runtime and function evaluation count for various configurations of SDC and MRSDC. Function evaluation counts are reported as: no. of advection/diffusion evaluations / no. of chemistry evaluations. The SRSDC  $X$  configuration uses single-rate SDC with  $X$  nodes. The MRSDC  $X / Y$  configurations use MRSDC with  $X$  coarse nodes and  $Y$  fine nodes between each pair of coarse nodes (type (b) in §3.2). The MRSDC  $X / Y \times R$  configurations use MRSDC with  $X$  coarse nodes and  $Y$  fine nodes repeated  $R$  times between each pair of coarse nodes (type (c) in §3.2). All SDC nodes are Gauss-Lobatto (GL) nodes.

SDC Configuration	$\Delta t$ ( $10^{-9}$ s)	Runtime (s)	Evaluations (AD/R)
SRSDC, 3 GL	6	130.6	561/561
MRSDC, 3 GL / 9 GL type (b)	30	44.1	113/897
MRSDC, 3 GL / 13 GL type (b)	42	39.7	81/961
MRSDC, 3 GL / $3 \times 8$ GL type (c)	60	30.8	57/897
MRSDC, 3 GL / $5 \times 2$ GL type (c)	60	21.7	57/449

40 atm everywhere. The initial temperature, velocity and mole fractions of species are set to

$$T_0 = \eta T_{\text{jet}} + (1 - \eta) T_{\text{air}}, \quad (31)$$

$$v_{0x} = 0, \quad (32)$$

$$v_{0y} = \eta v_{\text{jet}} + (1 - \eta) v_{\text{air}}, \quad (33)$$

$$X_0 = \eta X_{\text{jet}} + (1 - \eta) X_{\text{air}}, \quad (34)$$

where  $T_{\text{jet}} = 400$  K,  $T_{\text{air}} = 1525$  K,  $v_{\text{jet}} = 51.2$  m s $^{-1}$ , and  $v_{\text{air}} = 5.12$  m s $^{-1}$ . The  $\eta$  variable is given by

$$\eta = \frac{1}{2} \left( \tanh \frac{x + x_0}{\sigma} - \tanh \frac{x - x_0}{\sigma} \right), \quad (35)$$

where  $x_0 = 5.69 \times 10^{-5}$  m and  $\sigma = 0.5x_0$ . The mole fractions of species for the “jet” and “air” states are set to zero except that

$$X_{\text{jet}}(\text{CH}_3\text{OCH}_3) = 0.2, \quad (36)$$

$$X_{\text{jet}}(\text{N}_2) = 0.8, \quad (37)$$

$$X_{\text{air}}(\text{O}_2) = 0.21, \quad (38)$$

$$X_{\text{air}}(\text{N}_2) = 0.79. \quad (39)$$

An inflow boundary is used at the lower  $y$ -boundary, whereas outflow boundary conditions are applied at the other three boundaries. Sinusoidal variation is added to the inflow velocity as follows,

$$v_y(x, t) = v_{0y} + \tilde{v} \eta \sin \left( \frac{2\pi}{L_x} x \right) \sin \left( \frac{2\pi}{L_t} t \right), \quad (40)$$

where  $\tilde{v} = 10$  m s $^{-1}$ ,  $L_x = 0.00228$  m is the length of the domain in  $x$ -direction, and  $L_t = 10^{-5}$  s is the period of the variation. With these parameters, the resulting flow problem is in the low Mach number regime to facilitate cross-validation with an established low Mach number solver [9]

The 39-species DME mechanism used in this test is so stiff that it becomes impractical to evolve the reaction system explicitly. Hence, we use the variable-order BDF scheme in VODE [6] for computing species production rates. In this test, we use MRSDC, and put the reaction terms  $\rho \dot{\omega}_k$  in (1c) and advection-diffusion

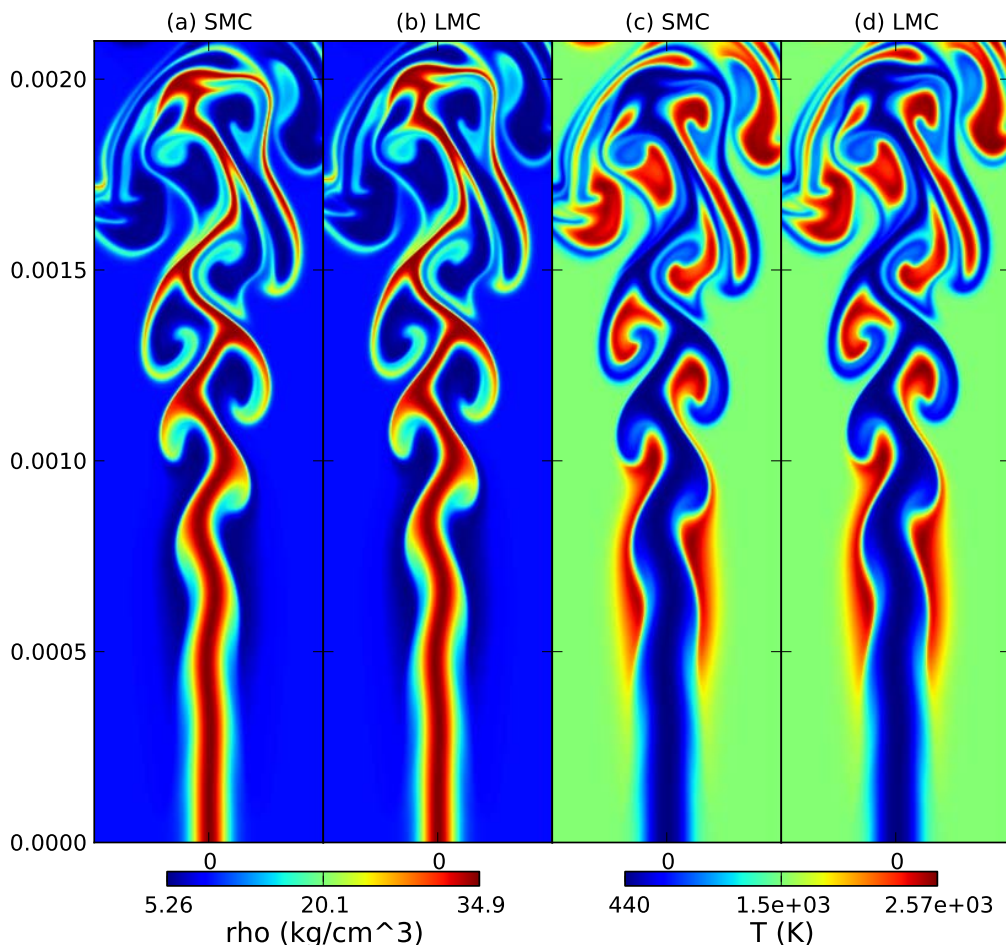


Figure 2. Density and temperature at  $6 \times 10^{-5}$  s for the DME jet test problem. We show (a) density from SMC, (b) density from LMC, (c) temperature from SMC, and (d) temperature from LMC. Only part of the domain immediately surrounding the jet is shown here.

terms on the coarse and fine nodes, respectively. Due to the use of an implicit solver, we can evaluate the reaction terms on the coarse node with a large time step without suffering from instability. As for advection-diffusion terms, the time step is limited by the acoustic time scale. In this test, we use 5 coarse Gauss-Lobatto nodes for the reaction terms, whereas for the advection-diffusion terms we use 3 fine Gauss-Lobatto nodes repeated twice between each pair of coarse nodes. The time step is chosen to have a Courant-Friedrichs-Lewy (CFL) number of 2. The effective CFL numbers for a substep of advection-diffusion (i.e., the interval spanned by 3 fine Gauss-Lobatto nodes) are about 0.17 and 0.33. (Note that the 5 coarse Gauss-Lobatto nodes are not evenly distributed.) We perform 4 SDC iterations per time step. The simulation is run with  $2048^2$  uniform points corresponding to a cell size of  $\sim 1.1 \times 10^{-6}$  m up to time  $6 \times 10^{-5}$  s. The numerical results are shown in figures 2 & 3. As a validation of SMC, we have also presented the numerical results obtained using the LMC code that is based on a low-Mach number formulation [4, 9, 26] that approximates the compressible flow equation to  $O(M^2)$ . The results of the two codes are in good agreement in spite of the difference between the two formulations. This is because the maximum Mach number  $M$  in this problem is only 0.14 so the low Mach number model is applicable.

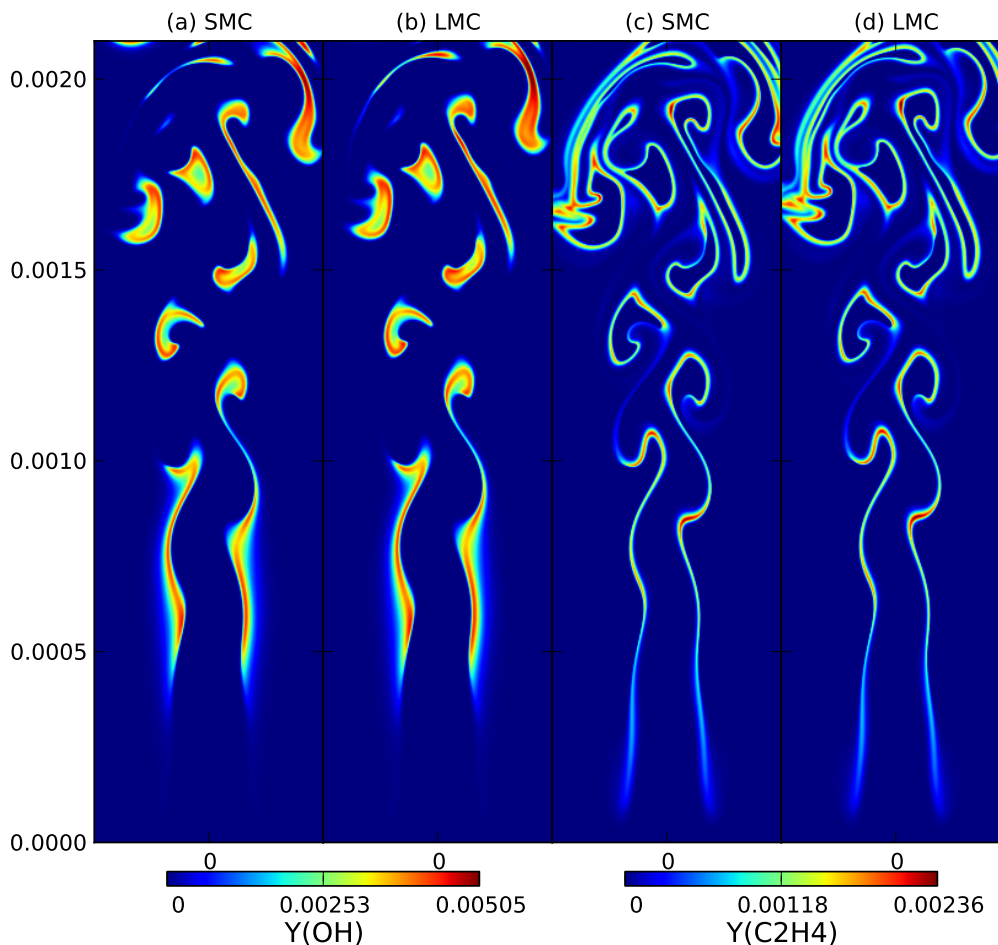


Figure 3. Mass fraction of OH and C<sub>2</sub>H<sub>4</sub> at  $6 \times 10^{-5}$  s for the DME jet test problem. We show (a)  $Y(\text{OH})$  from SMC, (b)  $Y(\text{OH})$  from LMC, (c)  $Y(\text{C}_2\text{H}_4)$  from SMC, and (d)  $Y(\text{C}_2\text{H}_4)$  from LMC. Only part of the domain immediately surrounding the jet is shown here.

## 6. Conclusions

We have described a numerical algorithm for integrating the multicomponent, reacting, compressible Navier-Stokes equations that is eight-order in space with fourth order to eighth order temporal integration. The methodology uses a narrow stencil approximation of diffusive terms that reduces the communication compared to existing methods and removes the need to use a filtering algorithm to remove Nyquist frequency oscillations that are not damped with traditional approaches. It also incorporates a multirate temporal integration strategy that provides an efficient mechanism for treating chemical mechanisms that are stiff relative to fluid dynamical time scales. The multirate integration approach supports two modes for operation. One treats the reactions explicitly using smaller time steps than are used for the fluid mechanics; the other treats reaction implicitly for case in which the chemical time scales are significantly faster than the fluid dynamical time scales. The implementation uses a hybrid programming model designed for effective utilization of a large number of threads that is targeted toward next generation many-core architectures. The code scales well to approximately 100K cores and shows excellent thread performance on a 61-core Intel Xeon Phi coprocessor. We present numerical results demonstrating the convergence properties of the algorithm with realistic chemical kinetics and validating the algorithm against results obtained with an established low Mach number solver.

## Acknowledgments

This work was supported by the Applied Mathematics Program and the Exascale Co-Design Program of the DOE Office of Advanced Scientific Computing Research under the U.S. Department of Energy under contract DE-AC02-05CH11231. This research used resources of the National Energy Research Scientific Computing Center, which is supported by the Office of Science of the U.S. Department of Energy under Contract No. DE-AC02-05CH11231.

## References

- [1] Center for Computational Sciences and Engineering, Lawrence Berkeley National Laboratory, *BoxLib*, software available at <https://ccse.lbl.gov/BoxLib/>.
- [2] G. BANSAL, A. MASCARENHAS, J. H. CHEN, T. LU, AND Z. LUO, *Direct numerical simulations of autoignition in stratified dimethyl-ether (dme)/air turbulent mixtures*, Combustion and Flame, in preparation (2013).
- [3] M. BAUM, T. J. POINSOT, D. C. HAWORTH, AND N. DARABIHA, *Direct numerical simulation of  $H_2/O_2/N_2$  flames with complex chemistry in two-dimensional turbulent flows*, J. Fluid Mech., 281 (1994), pp. 1–32.
- [4] J. B. BELL, M. S. DAY, A. S. ALMGREN, M. J. LIJEWSKI, AND C. A. RENDLEMAN, *Adaptive numerical simulation of turbulent premixed combustion*, in Proceedings of the first MIT conference on computational fluid and solid mechanics, Cambridge, MA, June 2001, MIT Press.
- [5] A. BOURLIOUX, A. T. LAYTON, AND M. L. MINION, *High-order multi-implicit spectral deferred correction methods for problems of reactive flow*, Journal of Computational Physics, 189 (2003), pp. 651–675.
- [6] P. BROWN, G. BYRNE, AND A. HINDMARSH, *Vode: A variable-coefficient ode solver*, SIAM Journal on Scientific and Statistical Computing, 10 (1989), pp. 1038–1051.
- [7] N. CHAKRABORTY AND S. CANT, *Unsteady effects of strain rate and curvature on turbulent premixed flames in an inflow-outflow configuration*, Combustion and Flame, 137 (2004), pp. 129 – 147.
- [8] J. H. CHEN AND H. IM, *Correlation of flame speed with stretch in turbulent premixed methane/air flames*, Proc. Combust. Inst., 27 (1998), pp. 819–826.
- [9] M. S. DAY AND J. B. BELL, *Numerical simulation of laminar reacting flows with complex chemistry*, Combust. Theory Modelling, 4 (2000), pp. 535–556.
- [10] A. DUTT, L. GREENGARD, AND V. ROKHLIN, *Spectral deferred correction methods for ordinary differential equations*, BIT Numerical Mathematics, 40 (2000), pp. 241–266.
- [11] A. ERN, C. C. DOUGLAS, AND M. D. SMOOKE, *Detailed chemistry modeling of laminar diffusion flames on parallel computers*, Int. J. Sup. App., 9 (1995), pp. 167–186.
- [12] A. ERN AND V. GIOVANGIOLI, *Multicomponent Transport Algorithms*, vol. m24 of Lecture Notes in Physics, Springer-Verlag, Berlin, 1994.
- [13] A. C. HANSEN AND J. STRAIN, *Convergence theory for spectral deferred correction*, Preprint, (2006).
- [14] D. C. HAWORTH AND T. J. POINSOT, *Numerical simulations of Lewis number effects in turbulent premixed flames*, J. Fluid Mech., 244 (1992), pp. 405–436.
- [15] J. HUANG, J. JIA, AND M. MINION, *Accelerating the convergence of spectral deferred correction methods*, Journal of Computational Physics, 214 (2006), pp. 633–656.
- [16] K. JENKINS AND R. CANT, *Direct numerical simulation of turbulent flame kernels*, in Recent Advances in DNS and LES, D. Knight and L. Sakell, eds., vol. 54 of Fluid Mechanics and its Applications, Springer Netherlands, 1999, pp. 191–202.
- [17] R. KAMAKOTI AND C. PANTANO, *High-order narrow stencil finite-difference approximations of second-order derivatives involving variable coefficients*, SIAM Journal on Scientific Computing, 31 (2010), pp. 4222–4243.
- [18] C. A. KENNEDY AND M. H. CARPENTER, *Several new numerical methods for compressible shear-layer simulations*, Applied Numerical Mathematics, 14 (1994), pp. 397 – 433.
- [19] C. A. KENNEDY, M. H. CARPENTER, AND R. M. LEWIS, *Low-storage, explicit runge-kutta schemes for the compressible navier-stokes equations*, Applied Numerical Mathematics, 35 (2000), pp. 177 – 219.
- [20] H. KOLLA, R. W. GROUT, A. GRUBER, AND J. H. CHEN, *Mechanisms of flame stabilization and blowout in a reacting turbulent hydrogen jet in cross-flow*, Combustion and Flame, 159 (2012), pp. 2755 – 2766. Special Issue on Turbulent Combustion.
- [21] A. T. LAYTON AND M. L. MINION, *Conservative multi-implicit spectral deferred correction methods for reacting gas dynamics*, Journal of Computational Physics, 194 (2004), pp. 697–715.
- [22] S. K. LELE, *Compact finite difference schemes with spectral-like resolution*, Journal of Computational Physics, 103 (1992), pp. 16 – 42.
- [23] J. LI, Z. ZHAO, A. KAZAKOV, AND F. L. DRYER, *An updated comprehensive kinetic model of hydrogen combustion*, International Journal of Chemical Kinetics, 36 (2004), pp. 566–575.
- [24] M. L. MINION, *Semi-implicit spectral deferred correction methods for ordinary differential equations*, Communications in Mathematical Sciences, 1 (2003), pp. 471–500.
- [25] ———, *Semi-implicit projection methods for incompressible flow based on spectral deferred corrections*, Applied numerical mathematics, 48 (2004), pp. 369–387.
- [26] A. NONAKA, J. B. BELL, M. S. DAY, C. GILET, A. S. ALMGREN, AND M. L. MINION, *A deferred correction coupling strategy for low mach number flow with complex chemistry*, Combustion Theory and Modelling, 16 (2012), pp. 1053–1088.

- [27] T. POINSOT, S. CANDEL, AND A. TROUV, *Applications of direct numerical simulation to premixed turbulent combustion*, Progress in Energy and Combustion Science, 21 (1995), pp. 531 – 576.
- [28] T. POINSOT AND S. LELEF, *Boundary conditions for direct simulations of compressible viscous flows*, Journal of Computational Physics, 101 (1992), pp. 104 – 129.
- [29] T. POINSOT AND D. VEYNANTE, *Theoretical and Numerical Combustion*, R. T. Edwards, Inc., Philadelphia, first ed., 2001.
- [30] R. SANKARAN, E. R. HAWKES, J. H. CHEN, T. LU, AND C. K. LAW, *Structure of a spatially developing turbulent lean methane-air bunsen flame*, Proceedings of the Combustion Institute, 31 (2007), pp. 1291 – 1298.
- [31] R. SANKARAN, E. R. HAWKES, C. Y. YOO, J. H. CHEN, T. LU, AND C. K. LAW, *Direct numerical simulation of stationary lean premixed methane-air flames under intense turbulence*, in Proceedings of the 5<sup>th</sup> US Combustion Meeting (CD-ROM), Western States Section of the Combustion Institute, Mar. 2007. Paper B09.
- [32] G. P. SMITH ET AL., *GRI-Mech 3.0*. Available at [http://www.me.berkeley.edu/gri\\_mech](http://www.me.berkeley.edu/gri_mech).
- [33] J. C. SUTHERLAND AND C. A. KENNEDY, *Improved boundary conditions for viscous, reacting, compressible flows*, Journal of Computational Physics, 191 (2003), pp. 502 – 524.
- [34] M. TANAHASHI, M. FUJIMURA, AND T. MIYAUCHI, *Coherent fine scale eddies in turbulent premixed flames*, Proc. Combust. Inst., 28 (2000), pp. 529–535.
- [35] K. W. THOMPSON, *Time dependent boundary conditions for hyperbolic systems*, Journal of Computational Physics, 68 (1987), pp. 1 – 24.
- [36] ———, *Time-dependent boundary conditions for hyperbolic systems, {II}*, Journal of Computational Physics, 89 (1990), pp. 439 – 461.
- [37] L. VERVISCH AND T. POINSOT, *Direct numerical simulation of non-premixed turbulent flames*, Annual Review of Fluid Mechanics, 30 (1998), pp. 655–691.
- [38] C. S. YOO AND H. G. IM, *Characteristic boundary conditions for simulations of compressible reacting flows with multi-dimensional, viscous and reaction effects*, Combustion Theory and Modelling, 11 (2007), pp. 259–286.
- [39] C. S. YOO, E. S. RICHARDSON, R. SANKARAN, AND J. H. CHEN, *A DNS study on the stabilization mechanism of a turbulent lifted ethylene jet flame in highly-heated coflow*, Proceedings of the Combustion Institute, 33 (2011), pp. 1619 – 1627.
- [40] C. S. YOO, Y. WANG, A. TROUV, AND H. G. IM, *Characteristic boundary conditions for direct simulations of turbulent counterflow flames*, Combustion Theory and Modelling, 9 (2005), pp. 617–646.